

MGS-SLAM: Monocular Sparse Tracking and Gaussian Mapping with Depth Smooth Regularization

Pengcheng Zhu^{1,2}, Yaoming Zhuang^{1,*}, Baoquan Chen¹, Li Li³,
Chengdong Wu¹, and Zhanlin Liu⁴

Abstract—This letter introduces a novel framework for dense Visual Simultaneous Localization and Mapping (VSLAM) based on Gaussian Splatting. Recently Gaussian Splatting-based SLAM has yielded promising results, but rely on RGB-D input and is weak in tracking. To address these limitations, we uniquely integrates advanced sparse visual odometry with a dense Gaussian Splatting scene representation for the first time, thereby eliminating the dependency on depth maps typical of Gaussian Splatting-based SLAM systems and enhancing tracking robustness. Here, the sparse visual odometry tracks camera poses in RGB stream, while Gaussian Splatting handles map reconstruction. These components are interconnected through a Multi-View Stereo (MVS) depth estimation network. And we propose a depth smooth loss to reduce the negative effect of estimated depth maps. Furthermore, the consistency in scale between the sparse visual odometry and the dense Gaussian map is preserved by Sparse-Dense Adjustment Ring (SDAR). We have evaluated our system across various synthetic and real-world datasets. The accuracy of our pose estimation surpasses existing methods and achieves state-of-the-art performance. Additionally, it outperforms previous monocular methods in terms of novel view synthesis fidelity, matching the results of neural SLAM systems that utilize RGB-D input.

I. INTRODUCTION

Simultaneous Localization and Mapping (SLAM) is a key technology in robotics and autonomous driving. It aims to solve the problem of how robots determine their location and reconstruct maps of the environment in unknown scenes. The development of SLAM technology has gone through multiple stages, starting with the initial filter-based methods [1], [2], advancing to graph optimization-based methods[3], [4], and more recently, integrating deep learning. This integration has significantly improved the accuracy and robustness of SLAM systems. With the rapid development of deep learning technology, a new approach to SLAM technology has emerged, utilizing differentiable rendering. The initial applications of differentiable rendering-based SLAM utilized Neural Radiance Fields (NeRF) as their foundational construction method. NeRF, as detailed in [5], employs neural networks to represent 3D scenes, enabling the synthesis of high-quality images and the recovery of dense geometric structures from multiple views. NeRF-based SLAM systems preserve detailed scene information during

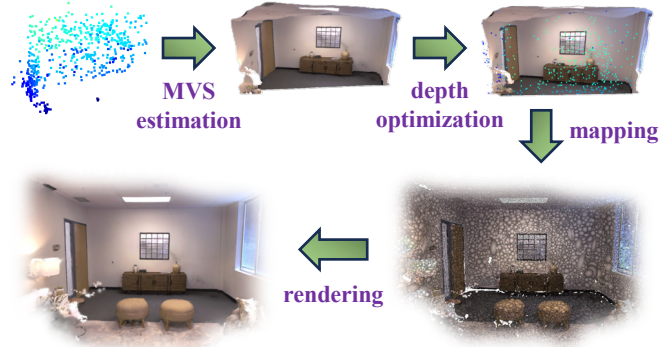


Fig. 1. Map reconstruction process by the proposed system. The prior depth map is estimated from the keyframes of sparse visual odometry and optimized by a sparse point cloud map, and the optimized depth map is used to construct a dense Gaussian map.

mapping, which enhances support for subsequent navigation and path planning. However, NeRF’s approach requires multiple forward predictions for each pixel during image rendering, leading to significant computational redundancy. Consequently, this inefficiency prevents NeRF-based SLAM from operating in real-time, thus limiting its practicality for immediate downstream tasks.

Recently, a novel scene representation framework called 3D Gaussian Splatting [6] has demonstrated superior performance compared to NeRF. It features a more concise scene representation method and real-time rendering capability. 3D Gaussian Splatting represents the geometries in a scene using a smooth and continuously differentiable method. This representation method not only delivers an accurate description of the scene but also offers a differentiable approach for optimizing the scene and camera poses. This opens up a new research direction for differentiable rendering-based SLAM. However, current Gaussian Splatting-based SLAM systems rely on the depth maps input from RGB-D cameras, which constrains the scope of their application.

This letter presents MGS-SLAM, a novel monocular Gaussian Splatting-based SLAM system. This work introduces several groundbreaking advancements in the field of SLAM, which include integrating Gaussian Splatting-based techniques with sparse visual odometry, employing a pre-trained Multi-View Stereo (MVS) depth estimation network, pioneering a geometric smooth depth loss, and developing the Sparse-Dense Adjustment Ring (SDAR) to ensure scale consistency. Together, these innovations significantly improve the accuracy and functionality of SLAM systems that rely solely on RGB images input. Fig. 1 illustrates the

*Corresponding author (email: zhuangyaoming@mail.neu.edu.cn).

¹Faculty of Robot Science and Engineering, Northeastern University, Shenyang 110819, China.

²College of Information Science and Engineering, Northeastern University, Shenyang 110819, China.

³JangHo School of Architecture, Northeastern University, Shenyang 110819, China.

⁴AstrumU, Bellevue, Washington, 98004, USA.

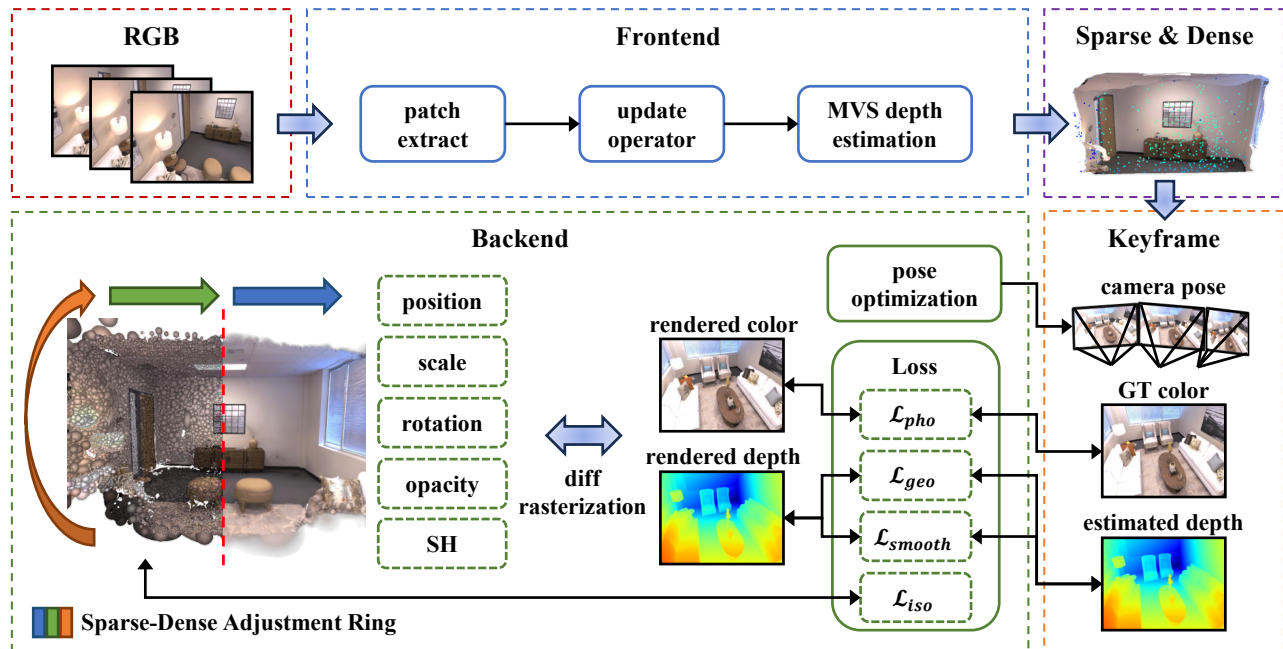


Fig. 2. **System pipeline.** The system inputs an RGB stream and operates frontend and backend processes in parallel. In the frontend, sparse visual odometry extracts patch features from images to estimate poses. These estimated poses and images are inputs to a pre-trained Multi-View Stereo (MVS) network, which estimates priori depth maps. In the backend, the estimated priori depth maps and images, coupled with poses from the frontend, are utilized as supervisory information to construct a Gaussian map. The frontend and backend maintain scale consistency through the Sparse-Dense Adjustment Ring (SDAR) strategy.

map construction process: initially, sparse visual odometry constructs the sparse map; subsequently, the MVS depth estimation network generates priori depth maps; this depth maps, along with the sparse point map, is then refined through depth optimization in the SDAR; and finally, the Gaussian map is constructed using the optimized priori depth maps and depth smooth regularization loss.

The key contributions of the proposed system are summarized as follows:

- Introducing the first SLAM system that combines sparse visual odometry with 3D Gaussian Splatting to achieve the construction of a dense Gaussian map using only RGB images as input.
- Developing a pre-trained Multi-View Stereo (MVS) depth estimation network that utilizes sparse odometry keyframes and their poses to estimate prior depth maps, thus providing crucial geometric constraints for Gaussian map reconstruction.
- Proposing a geometric depth smooth loss method to minimize the adverse impacts of inaccuracies in estimated prior depth maps on the Gaussian map and guide its alignment to correct geometric positions.
- Proposing a Sparse-Dense Adjustment Ring (SDAR) strategy to unify the scale consistency of sparse visual odometry and dense Gaussian map.

II. RELATED WORKS

Monocular Dense SLAM. Over the past few decades, monocular dense SLAM technology has seen significant advancements. DTAM [7] pioneered one of the earliest real-time dense SLAM systems by performing parallel depth

computations on GPU. To balance computational costs and accuracy, there are also semi-dense methods such as [8], [9], but these methods struggle to capture areas with poor texture. In the era of deep learning, DROID-SLAM [10] utilizes optical flow networks to establish dense pixel correspondences and achieve precise pose estimation. Another study [11], [12] combines a real-time VO/SLAM system with a Multi-View Stereo (MVS) network for parallel tracking and dense depth estimation, and then the Truncated Signed Distance Function (TSDF) [13] is used to fuse depth maps and extract mesh. [14] and [15] incorporate sparse point cloud correction and volumetric fusion strategy on the estimated depth map to mitigate the impact of errors in the estimated depth map. We have also adopted a strategy for correcting the estimated depth map, but the difference is that we use a linear variance correction as depth optimization, which is less computations.

Differentiable Rendering SLAM. With the emergence of Neural Radiance Fields (NeRF) in 2020, numerous NeRF-based SLAM works have been proposed. iNerf [16] was the first to propose optimizing camera poses within a fixed NeRF reconstruction scene, which initiated the SLAM adaptation of NeRF. iMAP [17] represented the pioneering work in NeRF-based SLAM, utilizing a dual-threading mode to track camera poses and execute mapping simultaneously. NICE-SLAM [18] introduced feature grids based on iMAP, enabling NeRF-based SLAM to represent larger scenes. Subsequent works such as GO-SLAM [19], HI-SLAM [20], and Loopy-SLAM [21] incorporated global bundle adjustment (BA) and loop closure correction, further enhancing pose estimation accuracy and mapping performance. Recently, 3D Gaussian Splatting has shown superior performance in

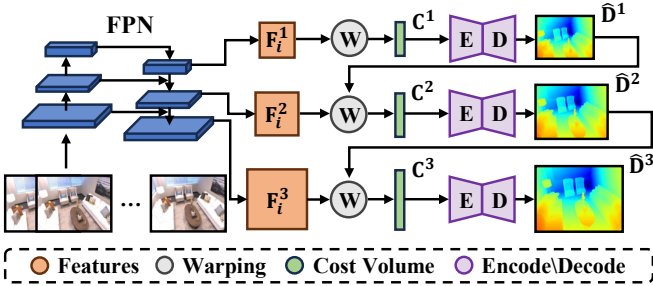


Fig. 3. The priori depth estimation network. The inputs to the network is images with poses from sparse visual odometry, image features are extracted by Feature Pyramid Network (FPN) and warping to 2D cost volume. Finally, encoded and decoded to depth maps using coarse-to-fine strategy.

3D scene representation, with its fast rendering capability and Gaussian scene representation being more suitable for online systems like SLAM. SplaTAM [22] combines 3D Gaussian Splatting with SLAM, leveraging the realistic scene reconstruction ability of 3D Gaussian Splatting to surpass NeRF-based SLAM methods in rendering quality. MonoGS [23] achieves monocular map reconstruction of Gaussian Splatting-based SLAM in small scenes through a map clipping strategy. However, existing Gaussian Splatting-based SLAM implementations typically require depth maps input from RGB-D sensors, and their monocular methods are often unable to operate effectively on larger datasets, such as Replica [24]. We propose the system utilizing only RGB images as input and demonstrated enhanced robustness by successfully operating on the Replica dataset.

III. METHODS

Our approach utilizes RGB images as input, parallelly performing camera poses estimation and photorealistic dense mapping. As depicted in Fig. 2, the core idea of the approach is to use a pre-trained Multi-View Stereo (MVS) network to couple monocular sparse visual odometry and dense Gaussian Splatting mapping and to maintain scale consistency between sparse point cloud map and dense Gaussian map by the Sparse-Dense Adjustment Ring (SDAR). Specifically, in the frontend part, tracking RGB images provides the backend with coarse camera poses and priori depth maps (Sec. III-A). In the backend part, represent the dense map using Gaussians, and jointly optimize the map and the coarse poses from the frontend (Sec. III-B). In the system components part, system initialization, selecting the keyframes for the system and correcting the scale between sparse point cloud map and dense Gaussian map by SDAR strategy are reported (Sec. III-C).

A. Sparse Visual Odometry Frontend

To achieve more accurate camera poses tracking and provide dense depth geometry before backend mapping, the frontend of our framework is built on the Deep Patch Visual Odometry (DPVO) [25] algorithm. DPVO is a learning-based sparse monocular visual odometry method for estimating camera poses and building sparse point cloud map by constructing and optimizing errors on patch graph. Given an input RGB stream, the scene is represented as a collection

of camera poses $\mathbf{T} \in SE(3)^N$ and a series of square image patches \mathbf{P} extracted from the images, and add them to the bi-directional patch graph that connects the patches to the frames. The projection of a square patch k taken from frame i in frame j can be formulated as:

$$\mathbf{P}_k^{ij} \sim \mathbf{K}\mathbf{T}_j\mathbf{T}_i^{-1}\mathbf{K}^{-1}\mathbf{P}_k^i \quad (1)$$

where \mathbf{K} refers to camera intrinsic matrix, $\mathbf{P}_k^i = [u, v, 1, d]^T$ denotes patch k in frame i , and $[u, v]$ denote the pixel coordinates in images, d denotes the inverse depth.

The core of DPVO is an update operator that computes the hidden state for each edge $(k, i, j) \in \varepsilon$. It optimize the reprojection errors on the patch graph to predict a 2D correction vector $\delta_k^{ij} \in \mathbb{R}^2$ and confidence weight $\psi_k^{ij} \in \mathbb{R}^2$. Bundle Adjustment (BA) is performed using optical flow correction as a constraint, with iterative updates and refinement of camera poses and patch depths achieved through the non-linear least squares method. The cost function for bundle adjustment is as follows:

$$\sum_{(k,i,j) \in \varepsilon} \|\mathbf{K}\mathbf{T}_j\mathbf{T}_i^{-1}\mathbf{K}^{-1}\mathbf{P}_k^i - [\bar{\mathbf{P}}_k^{ij} + \delta_k^{ij}]\|_{\psi_k^{ij}}^2 \quad (2)$$

where $\|\cdot\|_{\psi}$ represents Mahalanobis distance, $\bar{\mathbf{P}}$ denotes the centre of patch.

Multi-view priori depth estimation. The backend dense Gaussian mapping requires the supervision of geometric depth maps. Unlike the previous method [26], we use a pre-trained Multi-View Stereo (MVS) network to estimate priori depth maps on the keyframes window of DPVO, the network is shown in Fig. 3. Inspired by the monocular depth estimation method [27], our MVS network consists entirely of 2D convolutions with a coarse-to-fine structure that progressively refines the estimated priori depth map to reduce the runtime of the MVS network.

To be more specific, the frame currently tracked by the sparse visual odometry is used as the reference image \mathbf{I}^0 . Additionally, we employ the previous N keyframes as a series of original images $\mathbf{I}^{n \in 1, \dots, N}$. These images and their corresponding camera poses, serve as inputs to the MVS network. Utilizing the Feature Pyramid Network (FPN) module, we extract three layers of image features \mathbf{F}_i^s for each image, with s denoting the layer index and i representing the image index. Each layer contains image features with twice the length and width of the previous layer. In each layer, the image features of the original images dot the image feature of the reference image by a differentiable warping operation to obtain a cost volume with dimensions $\mathbf{D} \times \mathbf{H}^s \times \mathbf{W}^s$, and the priori depth map of each layer is obtained by 2D convolutions encoding and decoding. The estimated depth map of the previous layer is upsampled as the reference depth map of the next layer to reduce the number of depth samples in the next layer. Each layer performs similar encoding and decoding operations, The final depth map are estimated after three layers to achieve the coarse-to-fine effect. Our MVS depth estimation network is trained on the ScanNet dataset [28], with a scale-invariant loss function to accommodate the

relative poses of the sparse visual odometers:

$$\mathcal{L}_{si}^s = \sqrt{\frac{1}{H^s W^s} \sum_{i,j} (g_{i,j}^s)^2 - \frac{\lambda}{(H^s W^s)^2} \left(\sum_{i,j} g_{i,j}^s \right)^2} \quad (3)$$

where $g_{i,j}^s = \uparrow_{gt} \log \hat{D}_{i,j}^s - \log D_{i,j}^{gt}$. $D_{i,j}^{gt}$ denotes a ground truth depth map, which is aligned to the size of predicted depth $D_{i,j}^{gt}$ by an upsampling operation \uparrow_{gt} . λ is a constant 0.85.

In addition, the multi-view loss and the normal loss are added to the loss function to maintain geometric consistency of depth estimation:

$$\mathcal{L}_{mv}^s = \frac{1}{N H^s W^s} \sum_{n,i,j} \left| \uparrow_{gt} \log \mathbf{T}_{0n}(\hat{D}_{i,j}^s) - \log D_{n,i,j}^{gt} \right| \quad (4)$$

$$\mathcal{L}_{normal}^s = \frac{1}{2 H^s W^s} \sum_{i,j} (1 - \hat{N}_{i,j}^s \cdot N_{i,j}^s) \quad (5)$$

where \mathbf{T}_{0n} denotes the transformation matrix from the reference image to the original image n . $\hat{N}_{i,j}^s$ and $N_{i,j}^s$ respectively denote the prediction normals and ground truth normals. The final MVS depth estimation network loss is as follows:

$$\mathcal{L} = \sum_{s=0}^l \frac{1}{2^s} (\lambda_{si} \mathcal{L}_{si}^s + \lambda_{mv} \mathcal{L}_{mv}^s + \lambda_{normal} \mathcal{L}_{normal}^s) \quad (6)$$

where l is 2, and we assign the loss weights λ_{si} , λ_{mv} and λ_{normal} to 1.0, 0.2 and 1.0 respectively.

B. 3D Gaussian Splatting Mapping Backend

The main responsibility of the backend is to further optimize the coarse poses from the frontend and map a Gaussian scene. The key to this thread is differentiable rendering and depth smooth regularisation loss, computing the loss between the renderings and the ground truth, and adjusting the coarse poses and Gaussian map by backward gradient propagation.

Differentiable Gaussian map representation. We use 3D Gaussian Splatting as a dense representation of the scene. 3D Gaussian Splatting is an efficient 3D spatial representation that maps scenes in a way similar to point clouds, avoiding the need to sample in the blank areas of the space like NeRF and having the ability to render in real-time. The influence of a single 3D Gaussian $p_i \in \mathbb{R}^3$ in 3D scene is as follows:

$$f(p_i) = \sigma(o_i) \cdot \exp\left(-\frac{1}{2}(p_i - \mu_i)^T \Sigma^{-1} (p_i - \mu_i)\right) \quad (7)$$

where $o_i \in \mathbb{R}$ denotes the opacity of the Gaussian, $\mu_i \in \mathbb{R}^3$ is the centre of the Gaussian, $\Sigma = R S S^T R^T \in \mathbb{R}^{3,3}$ is the covariance matrix computed with $S \in \mathbb{R}^3$ scaling and $R \in \mathbb{R}^{3,3}$ components. The expression for the projection of a 3D Gaussian onto the image plane is as follows:

$$\mu_I = \pi(\mathbf{T}_{CW} \cdot \mu_W) \quad (8)$$

$$\Sigma_I = J W \Sigma_W W^T J^T \quad (9)$$

where $\pi(\cdot)$ denotes the projection of the 3D Gaussian center, $\mathbf{T}_{CW} \in SE(3)$ is the the transformation matrix from world coordinate to camera coordinate in 3D space, J is a linear

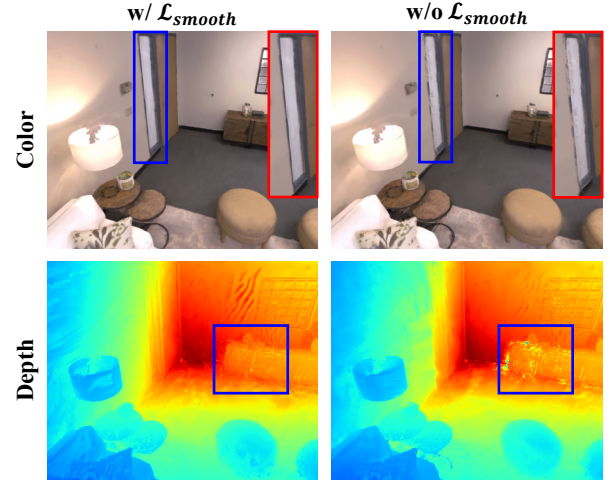


Fig. 4. Depth smooth regularization loss. Comparing the effect of having no depth smooth loss, there is better photometry and geometry in the left with depth smooth loss, and bad photometry and geometry in the right.

approximation to the Jacobian matrix of the projective transformation, W is the rotational component of \mathbf{T}_{CW} . The Eq. (8), (9) is differentiable, which ensures that the Gaussian map can be used with first-order gradient descent to continuously optimize the geometric and photometric of the map, allowing the map to be rendered as photo-realistic images. A single pixel color C_p is rendered from N Gaussians by splatting and blending:

$$C_p = \sum_{i \in N} c_i o_i \prod_{j=1}^{i-1} (1 - o_j) \quad (10)$$

where c_i is the color of Gaussian i , and o_i is the opacity of Gaussian i .

Mapping Optimization Losses. We changed the loss function of the original 3D Gaussian splatting and added more geometric constraints to make it more suitable for online mapping systems like SLAM. Specifically, our losses function consists of four components: photometric loss, depth geometric loss, depth smooth regularization loss and isotropic loss. In the photometric loss, the L1 loss is calculated between the rendered color image and the ground truth color image in the current camera pose \mathbf{T}_{CW} :

$$\mathcal{L}_{pho} = \|I(\mathcal{G}, \mathbf{T}_{CW}) - I^{gt}\|_1 \quad (11)$$

where $I(\mathcal{G}, \mathbf{T}_{CW})$ is the rendered color image from Gaussians \mathcal{G} , and I^{gt} is ground truth color image.

To improve the geometric accuracy of the Gaussian map, similar to Eq. (10), We also rendered the depth:

$$D_p = \sum_{i \in N} z_i o_i \prod_{j=1}^{i-1} (1 - o_j) \quad (12)$$

where z_i is the distance along the camera ray to the center μ_W of Gaussian i . Therefore, the depth geometric loss is as follows:

$$\mathcal{L}_{geo} = \|D(\mathcal{G}, \mathbf{T}_{CW}) - \bar{D}_d\|_1 \quad (13)$$

where $D(\mathcal{G}, \mathbf{T}_{CW})$ is the rendered depth map from Gaussians \mathcal{G} , \bar{D}_d is the optimized priori depth map by SDAR strategy. The optimization process is in Sec. III-C.

The prior depth maps obtained from the MVS network may not be entirely accurate. As depicted in Fig. 4, direct utilization of this depth maps lead to erroneous guidance in the geometric reconstruction of the Gaussian map. Therefore, we introduce the depth smooth regularization loss:

$$\mathcal{L}_{smooth} = \|d_{i,j-1} - d_{i,j}\|_2 + \|d_{i+1,j} - d_{i,j}\|_2 \quad (14)$$

where $d_{i,j}$ denotes the depth value of the pixel coordinate at (i, j) in the rendering depth map, it reduces the effect of errors in priori depth maps by regularizing neighboring pixels in rendered depth maps.

The original 3D Gaussian Splatting algorithm places no constraints on the Gaussians in the ray direction along the viewpoint. This has no effect on 3D reconstruction with fixed viewpoints. However, SLAM is an online mapping system, so this causes the Gaussians to elongate along the direction of the view ray, leading to the appearance of artifacts. To solve this problem, as well as [23], we also introduce isotropic loss:

$$\mathcal{L}_{iso} = \sum_{i=1}^{|\mathcal{G}|} \|s_i - \bar{s}_i \cdot 1\|_1 \quad (15)$$

where s_i is the scaling of Gaussians, suppressing the elongation of the Gaussians by regularizing both the scaling and mean \bar{s}_i . The final mapping optimization loss function is as follows:

$$\mathcal{L} = \lambda_p \mathcal{L}_{pho} + \lambda_g \mathcal{L}_{geo} + \lambda_s \mathcal{L}_{smooth} + \lambda_i \mathcal{L}_{iso} \quad (16)$$

where we assign the loss weights λ_p , λ_g , λ_s and λ_i to 0.99, 0.01, 1.0 and 1.0 respectively.

Camera poses optimization from the Gaussian map.

We use the camera pose \mathbf{T}_{CW}^S obtained from sparse visual odometry tracking in the frontend as the initial pose for Gaussian mapping in the backend. As in Eq. (10) and Eq. (12), we render the color image and depth map from the Gaussian map at the viewpoint of the current initial pose and compute the losses of renderings and the ground truth. Since this process is differentiable, the loss gradient is propagated to both the Gaussian map and the initial pose during the gradient backward process. The equation of the initial pose optimization update is as follows:

$$\arg \min_{\mathbf{T}_{CW}^S, \mathcal{G}} \mathcal{L}_{mapping}(\mathcal{G}, \mathbf{T}_{CW}^S, I^{gt}, \bar{D}_d) \quad (17)$$

where $\mathcal{L}_{mapping}$ is the Eq. (16), I^{gt} and \bar{D}_d is ground truth color image and optimized priori depth map from the viewpoint of \mathbf{T}_{CW}^S . Minimize the mapping loss to optimize both Gaussians \mathcal{G} and initial pose \mathbf{T}_{CW}^S simultaneously.

C. System Components

System initialization. Similar to DPVO, The system uses 8 frames for initialization. The pose of the new frame is initialized using a constant velocity motion model. Adding new patches and frames until 8 frames are accumulated and then running 12 iterations of the update operator. The 8 frames in the initialization are used as MVS network inputs to estimate the priori depth of the first frame. The backend

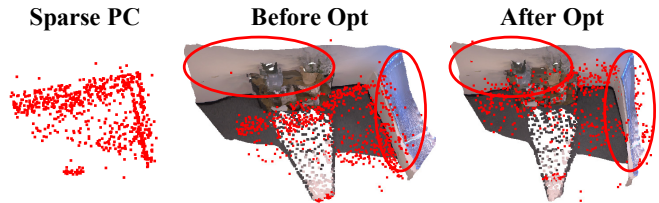


Fig. 5. Prior depth optimization. this optimization strategy in the SDAR is to correct the geometry of the priori depth map from MVS network and align the scale with the sparse point cloud map.

uses the first priori depth as the foundation to initialize the Gaussian map.

Keyframe selection. In the frontend tracking process, we always consider the 3 most recent frames as keyframes to fulfill the constant velocity motion model requirement. However, these 3 frames are not utilized for Gaussian mapping. Instead, we assess whether 4th frame satisfies Gaussian covisibility criteria. If it does, we add it into the mapping process in the backend; otherwise, we discard this frame. Between two keyframes i, j , we define the covisibility using Intersection of Union (IOU):

$$IOU_{cov}(i, j) = \frac{|\mathcal{G}_i \cap \mathcal{G}_j|}{|\mathcal{G}_i \cup \mathcal{G}_j|} \quad (18)$$

where $\mathcal{G}_i, \mathcal{G}_j$ are visible Gaussians in the viewpoints of frame i and frame j .

Sparse-Dense Adjustment Ring. We propose the Sparse-Dense Adjustment Ring (SDAR) strategy to achieve scale unification of the system. The method consists of three parts is as follows:

Firstly, We use a sparse point cloud map with better geometric accuracy to correct the priori depth map from the MVS network estimate. Specifically, the sparse point cloud is transformed to the camera coordinate where the priori depth map is located, and then the sparse point cloud is projected to the sparse depth map. The priori depth map and the sparse depth map conform to the normal distribution of $\hat{D}_d \sim \mathcal{N}(\mu_d, \sigma_d^2)$ and $D_s \sim \mathcal{N}(\mu_s, \sigma_s^2)$. Align the priori depth map with the sparse depth map using the following equation:

$$\bar{D}_d = \frac{\sigma_s}{\hat{\sigma}_d} \hat{D}_d + \mu_d \left(\frac{\mu_s}{\hat{\mu}_d} - \frac{\sigma_s}{\hat{\sigma}_d} \right) \quad (19)$$

where $\hat{\sigma}_d$ and $\hat{\mu}_d$ are the mean and standard deviation statistics of the sparsified priori depth map extracted from \hat{D}_d at the pixel coordinates of D_s . This strategy corrects the prior depth errors and maintains the scale consistency, as shown in Fig. 5.

Secondly, we backproject the optimized prior depth map with RGB color into space, generating a new point cloud. Subsequently, downsampling is performed on this new point cloud. New Gaussians are then initialized with the downsampled point cloud as the center and added to the Gaussian map. This operation ensures consistent scale between the Gaussian map and the sparse point cloud map, while downsampling helps mitigate errors in the prior depth map.

Finally, to achieve scale closure, we leverage the real-time rendering capability of the Gaussian map to generate the

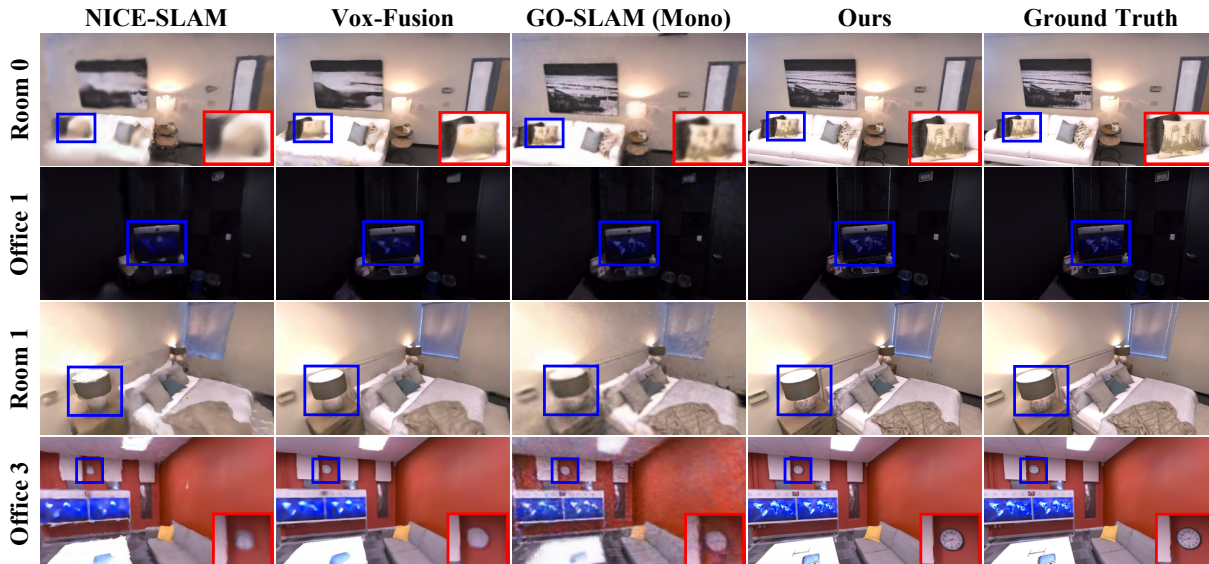


Fig. 6. The results of novel view rendering demonstrate the visualization outcomes on the Replica dataset for the proposed MGS-SLAM and other methods. Our system consistently generates significantly higher-quality and more realistic images than other monocular and RGB-D methods. This observation is further supported by quantitative results in Tab. III.

TABLE I
ATE [CM] RESULTS ON TUM DATASET

Input	Method	fr1/desk	fr2/xyz	fr3/office	Avg.
RGB-D	iMAP	4.90	2.00	5.80	4.23
	NICE-SLAM	4.26	6.19	6.87	5.77
	Vox-Fusion	3.52	1.49	26.01	10.34
	SplaTAM	3.35	1.24	5.16	3.25
Mono.	DSO	22.40	1.10	9.50	11.00
	DROID-VO	5.20	10.70	7.30	7.73
	DPVO	3.80	0.54	7.00	3.78
	MonoGS	4.15	4.79	4.39	4.44
	Ours	2.33	0.44	3.00	1.92

TABLE II
ATE [CM] RESULTS ON REPLICA DATASET

Input	Method	R0	R1	R2	O0	O1	O2	O3	O4	Avg.
RGB-D	iMAP	3.12	2.54	2.31	1.69	1.03	3.99	4.05	1.93	2.58
	NICE-SLAM	0.97	1.31	1.07	0.88	1.00	1.06	1.10	1.13	1.07
	Vox-Fusion	1.37	4.70	1.47	8.48	2.04	2.58	1.11	2.94	3.09
	SplaTAM	0.31	0.40	0.29	0.47	0.27	0.29	0.32	0.55	0.36
Mono.	DROID-VO	0.50	0.70	0.30	0.98	0.29	0.84	0.45	1.53	0.70
	NICE-SLAM	1.36	1.60	1.14	2.12	3.23	2.12	1.42	2.01	1.88
	DPVO	0.49	0.54	0.54	0.77	0.36	0.57	0.46	0.57	0.54
	MonoGS	9.94	×	×	×	×	×	11.58	×	10.76
	Ours	0.36	0.35	0.32	0.35	0.28	0.26	0.32	0.34	0.32

depth map of the frame being tracked at the frontend. We then initialize the depth of the tracking frame’s point cloud using this depth map. This strategy ensures that the frontend track aligns with the scale of the backend Gaussian map, facilitating the transfer of scale consistency from the backend to the frontend.

IV. EXPERIMENTS

We evaluate our proposed system on a series of real and synthetic datasets, including the TUM dataset [29] and the Replica dataset [24]. We compare the pose estimation accuracy (ATE) and Novel View Rendering quality with previous works, utilizing experimental results from papers

or open-source code of these works. The experimental data from the source code represents the average of three runs. Additionally, we conduct an ablation study to demonstrate the effectiveness of the components of our system. Finally, we analyze the system runtime.

A. Implementation Details

We evaluate our proposed system and other methods on a desktop with an Intel Core i7 12700 processor running at 3.60GHz and a single NVIDIA GeForce RTX 3090. The size of input images is consistent with the dataset size in our system, but these images are resized to 512×384 when estimating prior depth maps to better align with the resolution of MVS training images and enhance efficiency. Similar to Gaussian Splatting, mapping rasterization and gradient computations are implemented using CUDA. The remainder of our system pipeline is developed with PyTorch. For map optimization, we set the maximum gradient threshold to 0.0002 and the minimum opacity threshold to 0.65 for the Gaussians in the densify and prune operation of the mapping.

B. Camera Tracking Accuracy

For camera tracking accuracy, we report the Root Mean Square Error (RMSE) of the keyframes Absolute Trajectory Error (ATE). We benchmark our system against other approaches that, like ours, do not have explicit loop closure. We compared not only the monocular methods but also the RGB-D methods. The comparative work is very comprehensive including traditional direct visual odometry [9], learning-based SLAM[10], neural implicit slam [26], [30], and more recently Gaussian Splatting-based SLAM [22], [23].

Tab. I shows the tracking results on the TUM dataset. The tracking accuracy of SplaTAM exceeds other RGB-D methods. The tracking accuracy of our system also outperforms other monocular methods by 40%, while surpassing

TABLE III

RENDERING PERFORMANCE ON REPLICA DATASET. BEST RESULTS ARE HIGHLIGHTED AS **FIRST**, **SECOND**, AND **THIRD**

Method	Metric	R0	R1	R2	O0	O1	O2	O3	O4	Avg.
NICE-SLAM	PSNR[dB]↑	22.12	22.47	24.52	29.07	30.34	19.66	22.23	24.94	24.42
	SSIM↑	0.689	0.757	0.814	0.874	0.886	0.797	0.801	0.856	0.809
	LPIPS↓	0.330	0.271	0.208	0.229	0.181	0.235	0.209	0.198	0.233
Vox-Fusion	PSNR[dB]↑	22.39	22.36	23.92	27.79	29.83	20.33	23.47	25.21	24.41
	SSIM↑	0.683	0.751	0.798	0.857	0.876	0.794	0.803	0.847	0.801
	LPIPS↓	0.303	0.269	0.234	0.241	0.184	0.243	0.213	0.199	0.236
GO-SLAM	PSNR[dB]↑	23.25	20.70	21.08	21.44	22.59	22.33	22.19	22.76	22.04
	SSIM↑	0.712	0.739	0.708	0.761	0.726	0.740	0.752	0.722	0.733
	LPIPS↓	0.222	0.492	0.317	0.319	0.269	0.434	0.396	0.385	0.354
NICER-SLAM	PSNR[dB]↑	25.33	23.92	26.12	28.54	25.86	21.95	26.13	25.47	25.41
	SSIM↑	0.751	0.771	0.831	0.866	0.852	0.820	0.856	0.865	0.827
	LPIPS↓	0.250	0.215	0.176	0.172	0.178	0.195	0.162	0.177	0.191
MonoGS	PSNR[dB]↑	25.11	24.66	22.30	28.76	29.17	23.74	23.66	23.99	25.17
	SSIM↑	0.790	0.790	0.843	0.884	0.852	0.840	0.855	0.863	0.840
	LPIPS↓	0.260	0.360	0.351	0.293	0.274	0.290	0.216	0.340	0.298
Ours	PSNR[dB]↑	25.37	27.29	29.64	34.85	34.32	28.17	26.64	32.88	29.90
	SSIM↑	0.796	0.825	0.886	0.932	0.930	0.890	0.855	0.933	0.881
	LPIPS↓	0.153	0.072	0.071	0.069	0.098	0.112	0.086	0.079	0.093

TABLE IV

MAPPING LOSSES ABLATION ON OFFICE 0

\mathcal{L}_{geo}	\mathcal{L}_{smooth}	\mathcal{L}_{iso}	ATE[cm]↓	PSNR[dB]↑	Depth L1[cm]↓
✗	✗	✗	0.53	31.21	25.46
✓	✗	✗	0.45	33.80	11.09
✓	✓	✗	0.40	33.88	7.21
✓	✓	✓	0.35	34.85	5.37

TABLE V

SPARSE-DENSE ADJUSTMENT RING ABLATION ON OFFICE 0

Comp. 1	Comp. 2	Comp. 3	ATE[cm]↓	PSNR[dB]↑	Depth L1[cm]↓
✗	✗	✗	0.61	28.66	15.55
✓	✗	✗	0.49	29.53	11.01
✓	✓	✗	0.41	33.22	5.56
✓	✓	✓	0.35	34.85	5.37

SplaTAM. Tab. II shows the tracking results on the Replica dataset. The same Gaussian Splatting-based MonoGS with monocular input experienced tracking loss in some scenes in the Replica dataset. Our system completes the full scene tracking, demonstrates robustness, and achieves state-of-the-art tracking results. In addition, The experimental data from both tables show that our tracking performance is superior to the DPVO on which the frontend is based. This demonstrates the effectiveness of our combination of sparse visual odometry and Gaussian mapping to achieve a more robust and accurate SLAM system.

C. Novel View Rendering

We evaluated the methods for novel view rendering on Replica. To evaluate map quality, we report standard photometric rendering quality metrics (PSNR, SSIM and LPIPS) following the evaluation protocol used in [31]. The methods we are comparing have RGB-D input and monocular input. NICE-SLAM and Vox-Fusion are RGB-D input and the rest are monocular input. The rendering results of MonoGS is the average before it tracking loss. Tab. III shows the results, our proposed system performs state-of-the-art in most scenes. The visualisation of the rendering is shown in Fig. 6, where the quality of our rendered image is higher than the other methods and almost indistinguishable from the ground truth.

TABLE VI

RUNTIME ANALYSIS ON TUM FR3/OFFICE

Method	Tracking/Frame[s]	Mapping/Frame[s]	Total Time[s]	FPS
SplaTAM	3.65	1.44	10652	0.24
MonoGS	0.55	1.70~2.00	798.90	3.20
Ours	0.25	1.61~1.90	628.1	4.00

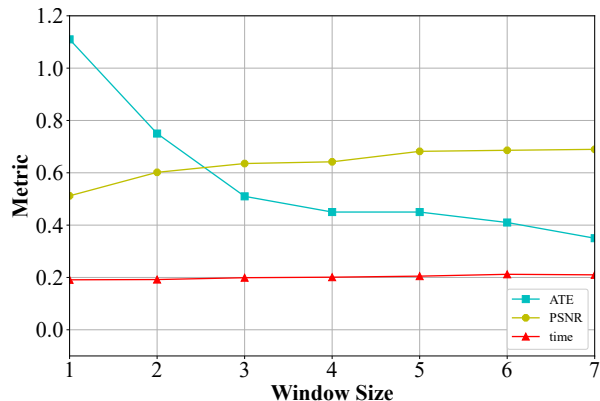


Fig. 7. MVS window analysis on Office 0. The MVS window size is a hyperparameter that allows for finding a balance between speed, tracking, and rendering quality. PSNR is divided by 50.

D. Ablative Analysis

Mapping losses ablation. We changed the losses function of the original 3D Gaussian Splatting by introducing depth loss, smooth loss, and isotropic loss. As shown in Tab. IV, we did an ablation study of these losses and evaluated their impact through ATE, PSNR, and Depth L1 metrics. The results show that all these losses contribute to the accuracy improvement of the system. It is worth noting that the depth loss utilizes the estimated priori depth map from the Network. Although this improves the geometry of our system, it also leads to incorrect geometric guidance. After adding the smooth loss, the geometric accuracy is further enhanced, proving that the smooth loss can correct some adverse effects of the estimated priori depth map.

Sparse-Dense Adjustment Ring ablation. We propose the Sparse-Dense Adjustment Ring (SDAR) strategy to unify the frontend and backend scales. This strategy comprises three components (Sec. III-C). We conducted an ablation study of these three components to demonstrate their effect on the system. The metrics for the ablation study are also adopted as PSNR, SSIM, and LPIPS. As shown in Tab. V, the contribution of SDAR to the system is mainly in the tracking accuracy ATE. The tracking accuracy of the system is similar to DPVO without the SDAR strategy. The tracking accuracy of the system is state-of-the-art with the SDAR strategy. This demonstrates the significance of combining sparse visual odometry and Gaussian mapping to build a more accurate and robust SLAM system.

MVS window analysis. Since the MVS network requires at least one reference frame and one source frame, the minimum window size is 2, and the maximum is the number of keyframes required for DPVO initialization. As depicted in Fig. 7, we have analyzed the effect of different window sizes of MVS on the accuracy and speed of the system.

Since our MVS network consists of 2D convolutions, increasing the window size has little effect on inference time. However, increasing the window size improves the system's tracking accuracy and mapping quality. This is because more keyframes with different views provide additional geometrical cues, which can estimate better prior depth map and enhance system accuracy.

E. Runtime Analysis

As shown in Tab. VI, we analyzed the runtime of our proposed system on the TUM fr3/office dataset and compared it to other methods. The results indicate we achieve higher frames per second (fps) than other Gaussian Splatting-based SLAM methods. This advantage is primarily attributed to the fast frontend tracking. These findings underscore the effectiveness of our approach, which combines sparse visual odometry and Gaussian mapping.

V. CONCLUSIONS

This letter introduces MGS-SLAM, a novel Gaussian Splatting-based SLAM framework. For the first time, our framework integrates sparse visual odometry with Gaussian mapping, addressing the tracking loss issue in larger scenes encountered by Gaussian Splatting-based SLAM and eliminating the need for depth maps input. We develop a lightweight MVS depth estimation network to facilitate this integration. Additionally, we propose the Sparse-Dense Adjustment Ring (SDAR) strategy to adjust the scale between the sparse map and the Gaussian map. Comparative evaluations demonstrate that our approach achieves state-of-the-art accuracy compared to previous methods.

REFERENCES

- [1] A. J. Davison, I. D. Reid, N. D. Molton, and O. Stasse, "Monoslam: Real-time single camera slam," *IEEE transactions on pattern analysis and machine intelligence*, vol. 29, no. 6, pp. 1052–1067, 2007.
- [2] G. Klein and D. Murray, "Parallel tracking and mapping for small ar workspaces," in *2007 6th IEEE and ACM international symposium on mixed and augmented reality*. IEEE, 2007, pp. 225–234.
- [3] R. Mur-Artal, J. M. M. Montiel, and J. D. Tardos, "Orb-slam: a versatile and accurate monocular slam system," *IEEE transactions on robotics*, vol. 31, no. 5, pp. 1147–1163, 2015.
- [4] R. Mur-Artal and J. D. Tardos, "Orb-slam2: An open-source slam system for monocular, stereo, and rgb-d cameras," *IEEE transactions on robotics*, vol. 33, no. 5, pp. 1255–1262, 2017.
- [5] B. Mildenhall, P. P. Srinivasan, M. Tancik, J. T. Barron, R. Ramamoorthi, and R. Ng, "Nerf: Representing scenes as neural radiance fields for view synthesis," *Communications of the ACM*, vol. 65, no. 1, pp. 99–106, 2021.
- [6] B. Kerbl, G. Kopanas, T. Leimkühler, and G. Drettakis, "3d gaussian splatting for real-time radiance field rendering," *ACM Transactions on Graphics*, vol. 42, no. 4, pp. 1–14, 2023.
- [7] R. A. Newcombe, S. J. Lovegrove, and A. J. Davison, "Dtam: Dense tracking and mapping in real-time," in *2011 international conference on computer vision*. IEEE, 2011, pp. 2320–2327.
- [8] J. Engel, T. Schöps, and D. Cremers, "Lsd-slam: Large-scale direct monocular slam," in *European conference on computer vision*. Springer, 2014, pp. 834–849.
- [9] J. Engel, V. Koltun, and D. Cremers, "Direct sparse odometry," *IEEE transactions on pattern analysis and machine intelligence*, vol. 40, no. 3, pp. 611–625, 2017.
- [10] Z. Teed and J. Deng, "Droid-slam: Deep visual slam for monocular, stereo, and rgb-d cameras," *Advances in neural information processing systems*, vol. 34, pp. 16 558–16 569, 2021.
- [11] R. Craig and R. C. Beavis, "Tandem: matching proteins with tandem mass spectra," *Bioinformatics*, vol. 20, no. 9, pp. 1466–1467, 2004.
- [12] X. Yang, L. Zhou, H. Jiang, Z. Tang, Y. Wang, H. Bao, and G. Zhang, "Mobile3drecon: Real-time monocular 3d reconstruction on a mobile phone," *IEEE Transactions on Visualization and Computer Graphics*, vol. 26, no. 12, pp. 3446–3456, 2020.
- [13] R. A. Newcombe, S. Izadi, O. Hilliges, D. Molyneaux, D. Kim, A. J. Davison, P. Kohi, J. Shotton, S. Hodges, and A. Fitzgibbon, "Kinectfusion: Real-time dense surface mapping and tracking," in *2011 10th IEEE international symposium on mixed and augmented reality*. Ieee, 2011, pp. 127–136.
- [14] H. Matsuki, R. Scona, J. Czarnowski, and A. J. Davison, "Codemapping: Real-time dense mapping for sparse slam using compact scene representations," *IEEE Robotics and Automation Letters*, vol. 6, no. 4, pp. 7105–7112, 2021.
- [15] A. Rosinol, J. J. Leonard, and L. Carlone, "Probabilistic volumetric fusion for dense monocular slam," in *Proceedings of the IEEE/CVF Winter Conference on Applications of Computer Vision*, 2023, pp. 3097–3105.
- [16] L. Yen-Chen, P. Florence, J. T. Barron, A. Rodriguez, P. Isola, and T.-Y. Lin, "inernf: Inverting neural radiance fields for pose estimation," in *2021 IEEE/RSJ International Conference on Intelligent Robots and Systems (IROS)*. IEEE, 2021, pp. 1323–1330.
- [17] E. Sucar, S. Liu, J. Ortiz, and A. J. Davison, "imap: Implicit mapping and positioning in real-time," in *Proceedings of the IEEE/CVF International Conference on Computer Vision*, 2021, pp. 6229–6238.
- [18] Z. Zhu, S. Peng, V. Larsson, W. Xu, H. Bao, Z. Cui, M. R. Oswald, and M. Pollefeys, "Nice-slam: Neural implicit scalable encoding for slam," in *Proceedings of the IEEE/CVF Conference on Computer Vision and Pattern Recognition*, 2022, pp. 12 786–12 796.
- [19] Y. Zhang, F. Tosi, S. Mattoccia, and M. Poggi, "Go-slam: Global optimization for consistent 3d instant reconstruction," in *Proceedings of the IEEE/CVF International Conference on Computer Vision*, 2023, pp. 3727–3737.
- [20] W. Zhang, T. Sun, S. Wang, Q. Cheng, and N. Haala, "Hi-slam: Monocular real-time dense mapping with hybrid implicit fields," *IEEE Robotics and Automation Letters*, 2023.
- [21] L. Liso, E. Sandström, V. Yugay, L. Van Gool, and M. R. Oswald, "Loopy-slam: Dense neural slam with loop closures," *arXiv preprint arXiv:2402.09944*, 2024.
- [22] N. Keetha, J. Karhade, K. M. Jatavallabhula, G. Yang, S. Scherer, D. Ramanan, and J. Luiten, "Splatam: Splat, track & map 3d gaussians for dense rgb-d slam," *arXiv preprint arXiv:2312.02126*, 2023.
- [23] H. Matsuki, R. Murai, P. H. Kelly, and A. J. Davison, "Gaussian splatting slam," *arXiv preprint arXiv:2312.06741*, 2023.
- [24] J. Straub, T. Whelan, L. Ma, Y. Chen, E. Wijmans, S. Green, J. J. Engel, R. Mur-Artal, C. Ren, S. Verma, *et al.*, "The replica dataset: A digital replica of indoor spaces," *arXiv preprint arXiv:1906.05797*, 2019.
- [25] Z. Teed, L. Lipson, and J. Deng, "Deep patch visual odometry," *Advances in Neural Information Processing Systems*, vol. 36, 2024.
- [26] Z. Zhu, S. Peng, V. Larsson, Z. Cui, M. R. Oswald, A. Geiger, and M. Pollefeys, "Nicer-slam: Neural implicit scene encoding for rgb slam," *arXiv preprint arXiv:2302.03594*, 2023.
- [27] C. Godard, O. Mac Aodha, and G. J. Brostow, "Unsupervised monocular depth estimation with left-right consistency," in *Proceedings of the IEEE conference on computer vision and pattern recognition*, 2017, pp. 270–279.
- [28] A. Dai, A. X. Chang, M. Savva, M. Halber, T. Funkhouser, and M. Nießner, "ScanNet: Richly-annotated 3d reconstructions of indoor scenes," in *Proceedings of the IEEE conference on computer vision and pattern recognition*, 2017, pp. 5828–5839.
- [29] J. Sturm, N. Engelhard, F. Endres, W. Burgard, and D. Cremers, "A benchmark for the evaluation of rgb-d slam systems," in *2012 IEEE/RSJ international conference on intelligent robots and systems*. IEEE, 2012, pp. 573–580.
- [30] X. Yang, H. Li, H. Zhai, Y. Ming, Y. Liu, and G. Zhang, "Vox-fusion: Dense tracking and mapping with voxel-based neural implicit representation," in *2022 IEEE International Symposium on Mixed and Augmented Reality (ISMAR)*. IEEE, 2022, pp. 499–507.
- [31] E. Sandström, Y. Li, L. Van Gool, and M. R. Oswald, "Point-slam: Dense neural point cloud-based slam," in *Proceedings of the IEEE/CVF International Conference on Computer Vision*, 2023, pp. 18 433–18 444.